

1 Original Article:

2 **Fusion of Video and Inertial Sensing Data via Dynamic**
3 **Optimization of a Biomechanical Model**

4
5
6 Owen Pearl, MS

7 Doctoral Student in Mechanical Engineering, Carnegie Mellon University, Pittsburgh, PA, USA

8 Soyong Shin, MS

9 Doctoral Student in Mechanical Engineering, Carnegie Mellon University, Pittsburgh, PA, USA

10 Ashwin Godura

11 Undergraduate Student in Electrical Engineering, Carnegie Mellon University, Pittsburgh, PA,

12 USA

13 Sarah Bergbreiter, PhD

14 Professor of Mechanical Engineering, Electrical Engineering, the Robotics Institute,

15 Carnegie Mellon University, Pittsburgh, PA, USA

16 Eni Halilaj, PhD

17 Assistant Professor of Mechanical Engineering, Biomedical Engineering, the Robotics Institute,

18 Carnegie Mellon University, Pittsburgh, PA, USA

19
20 Word Count: 3494

21 Submitted to *Journal of Biomechanics*

22 Please direct correspondence to: Eni Halilaj, PhD

23 Department of Mechanical Engineering, Carnegie Mellon University

24 5000 Forbes Ave, Pittsburgh, PA 15213

25 Email: ehalilaj@andrew.cmu.edu | Phone: 412-268-2183

26

ABSTRACT

27 Inertial sensing and computer vision are promising alternatives to traditional optical motion
28 tracking, but until now these data sources have been explored either in isolation or fused via
29 unconstrained optimization, which may not take full advantage of their complementary strengths.
30 By adding physiological plausibility and dynamical robustness to a proposed solution,
31 biomechanical modeling may enable better fusion than unconstrained optimization. To test this
32 hypothesis, we fused video and inertial sensing data via dynamic optimization with a nine degree-
33 of-freedom model and investigated when this approach outperforms video-only, inertial-sensing-
34 only, and unconstrained-fusion methods. We used both experimental and synthetic data that
35 mimicked different ranges of video and inertial measurement unit (IMU) data noise. Fusion with a
36 dynamically constrained model improved estimation of lower-extremity kinematics by a mean \pm
37 std root-mean-square error of $6.0^\circ \pm 1.2^\circ$ over the video-only approach and estimation of joint
38 centers by 4.5 ± 2.8 cm over the IMU-only approach. It consistently outperformed single-modality
39 approaches across different noise profiles. When the quality of video data was high and that of
40 inertial data was low, dynamically constrained fusion improved joint kinematics by $3.7^\circ \pm 1.2^\circ$ and
41 joint centers by 1.9 ± 0.5 cm over unconstrained fusion, while unconstrained fusion was
42 advantageous by $3.0^\circ \pm 1.4^\circ$ and 1.2 ± 0.7 cm in the opposite scenario. These findings indicate
43 that complementary modalities and techniques can improve motion tracking by clinically
44 meaningful margins and that data quality and computational complexity must be considered when
45 selecting the most appropriate method for a particular application.

46 **Key words:** kinematics, inertial measurement units, computer vision, direct collocation, simulation

47

1. INTRODUCTION

48 Accessible motion tracking could transform rehabilitation research and therapy. The traditional
49 marker-based approach is limited to specialized laboratories equipped with expensive optical
50 motion tracking systems and trained personnel. Inertial sensing and computer vision-based
51 approaches offer greater flexibility, given their low cost and portability, but collective
52 understanding of the strengths and weaknesses of kinematics estimation algorithms associated
53 with each technology is still evolving (Table 1). Additionally, efforts to merge the strengths of these
54 complementary technologies are sparse.

55

56 Vision-based methods are successful in camera-dense environments, but occlusion continues to
57 pose challenges in reduced-camera settings (Joo et al., 2019). Although now widely used in
58 robotics applications, translation of vision-based methods to human movement sciences remains
59 uncommon due to accuracy limitations (Seethapathi et al., 2019). Computer vision models are
60 data-driven and typically not constrained to satisfy physiological constraints. Biomechanical
61 modeling has been considered as a possible approach for improving the accuracy of computer
62 vision approaches and making them more accessible to the biomechanics community (Kanko et
63 al., 2021; Strutzenberger et al., 2021; Uhlrich et al., 2022). Although comparisons with marker-
64 based data suggest that the accuracy of these methods ranges widely between 3° – 20°,
65 depending on the degree-of-freedom, no study to date has systematically discerned how this
66 accuracy compares to alternative approaches and to what degree the incorporation of
67 biomechanical models improves results.

68

69 Similarly, converting multimodal time series data from inertial measurement units (IMU) into
70 accurate joint kinematics remains challenging due to the many possible sources of uncertainty,
71 including bias noise, thermo-mechanical white noise, flicker noise, temperature effects, calibration
72 errors, and soft-tissue artifacts (Park & Gao, 2008; Picerno, 2017). Traditional sensor fusion filters

73 used to mitigate drift (Madgwick, 2010; Mahony et al., 2008; Sabatini, 2011) typically rely on
74 magnetometers, which are susceptible to ferromagnetic interferences (de Vries et al., 2009). The
75 results of sensor-fusion filters have been refined with biomechanical models (Al Borno et al.,
76 2022), but whether findings will translate to natural environments remains uncertain because
77 marker-based motion capture was used for sensor-to-body calibration, IMUs impacted by
78 ferromagnetic disturbances were manually excluded, and the effect of soft-tissue motion was
79 partly eliminated by attaching IMUs to solid marker cluster plates, helping the IMUs move rigidly
80 with the marker clusters. Deep learning has been proposed as an alternative (Mundt et al., 2020;
81 Rapp et al., 2021), but the models have been limited by datasets that are not representative of
82 all activities and clinical populations. Constrained optimization via biomechanical modeling, both
83 static and dynamic, has also been used for estimation of both kinematics and kinetics. Static
84 optimization approaches rely on zero-velocity detection algorithms from joint constraints, external
85 contacts, and additional sensors (GPS, RF-based local positioning sensors, barometers, etc.) to
86 correct the position of the model at each step (Karatsidis et al., 2019; Roetenberg et al., 2013),
87 while dynamic optimization approaches currently require that the motion be periodic (Dorschky et
88 al., 2019), both of which limit ease of implementation and generalizability.

89

90 IMU and vision data have complementary strengths that can be leveraged to overcome their
91 individual limitations, but it is unclear if fusion via a dynamically constrained biomechanical model
92 would improve estimation of kinematics over unconstrained optimization (Halilaj et al., 2021).
93 Inertial sensing can compensate for occlusions in videos, videos can compensate for drift in
94 inertial data, and biomechanical models can add physiological plausibility and dynamical
95 robustness. Here we fuse video and IMU data via dynamic optimization of a nine degree-of-
96 freedom (DOF) model (Fig. 1) and investigate the circumstances under which this approach
97 outperforms (1) standard computer vision techniques using video data, (2) dynamic optimization
98 of a biomechanical model using IMU data, and (3) fusion of IMU and video data via unconstrained

99 optimization (i.e., without a biomechanical model). In addition to comparing these methods using
100 experimental data, we quantified their sensitivity to IMU and video data noise by scaling each
101 subject's unique noise backgrounds. We hypothesized that fusion of video and IMU data with
102 biomechanically constrained optimization would improve estimation of kinematics over the
103 alternatives under all the noise profiles. We have shared a MATLAB library to encourage testing
104 of these techniques with additional data and the exploration of new scientific questions.

105

106

2. METHODS

2.1 Biomechanical Model

108 The planar biomechanical model consisted of seven rigid body segments (Fig. 1). One segment
109 represented the head, arms, and torso and three segments represented each leg. Body-segment
110 lengths, masses, and mass moment of inertias were estimated by scaling a three-dimensional
111 musculoskeletal model based on 21 cadavers and 24 young adults (Delp et al., 1990, 2007) with
112 marker-based motion capture data. The model state, \mathbf{z} , contained nine general coordinates, \mathbf{q} ,
113 their generalized velocities, \mathbf{v} , consisting of the horizontal and vertical sagittal plane translation of
114 the pelvis, x and y , and the sagittal plane rotation of the pelvis, hip joints, knee joints, and ankle
115 joints, $q_t, q_{lh}, q_{rh}, q_{lk}, q_{rk}, q_{la}, q_{ra}$, respectively:

$$116 \quad \mathbf{z} = \begin{bmatrix} \mathbf{q} & \text{gen coords} \\ \mathbf{v} & \text{gen velocities} \end{bmatrix};$$

$$117 \quad \mathbf{q} = [x, y, q_t, q_{lh}, q_{rh}, q_{lk}, q_{rk}, q_{la}, q_{ra}]^T$$

118 The model control vector, \mathbf{u} , contained joint torques, \mathbf{T} , contact forces, \mathbf{F} , and residual forces
119 accounting for dynamic inconsistencies due to modeling simplifications, \mathbf{R} :

$$120 \quad \mathbf{u} = \begin{bmatrix} \mathbf{T} & \text{joint torques} \\ \mathbf{F} & \text{contact forces} \\ \mathbf{R} & \text{residual forces} \end{bmatrix};$$

121 $\mathbf{T} = [T_t, T_{lh}, T_{rh}, T_{lk}, T_{rk}, T_{la}, T_{ra}]^T;$

122 $\mathbf{F} = [F_{lx}, F_{ly}, F_{rx}, F_{ry}]^T;$

123 $\mathbf{R} = [R_x, R_y]^T$

124 We used Autolev (Symbolic Dynamics Inc; Sunnyvale, CA) and Kane's equations of motion to
125 derive symbolic expressions for the nine equations of motion in their explicit form and
126 implemented them in MATLAB (Mathworks, Inc; Natick, MA):

127 $\mathbf{z}' = f(\mathbf{z}, \mathbf{u})$

128

129 *2.2 Experimental Data*

130 To test the four markerless approaches for predicting joint kinematics, we used overground
131 walking data from five subjects (4 male; 1 female) from Total Capture (Fig. 2a), a publicly available
132 dataset commonly used to benchmark computer vision methods for motion tracking (Trumble et
133 al., 2017). Motion was captured in a 4 x 6 m area with eight high definition (HD) video cameras at
134 60 Hz, seven Xsens IMUs (Xsens; Enschede, The Netherlands) positioned on the pelvis, left and
135 right thigh, left and right shank, left and right foot at 1000 Hz, and a marker-based motion capture
136 system (Vicon Industries, Inc; Hauppauge, NY) at 100 Hz. Sagittal plane projections of the video
137 and IMU data were used as inputs for the biomechanical model.

138

139 *2.3 Kinematics Estimation: Vision-Only*

140 We extracted two-dimensional (2-D) keypoints (i.e., joint centers) and the confidence score
141 associated with each keypoint from each video camera using the Cascaded Pyramid Network
142 (CPN) (Chen et al., 2018). We triangulated the keypoints by using a direct linear transformation
143 algorithm to extract three-dimensional (3-D) keypoints (Hartley & Sturm, 1997). Contributions
144 from each video were weighted by the confidence score associated with the corresponding 2-D

145 keypoint. We computed kinematics by minimizing the error between the triangulated keypoints
 146 derived from video data and the joint centers of the biomechanical model.

147

148 *2.4 Kinematics Estimation: Dynamically Constrained Fusion*

149 Our proposed approach fuses video and IMU data by finding the model states $\mathbf{z}(t)$ and controls
 150 $\mathbf{u}(t)$ over time, such that the simulated keypoint locations and body segment accelerations and
 151 angular velocities from the model state match those obtained from experimental video and IMU
 152 data. This was done by formulating the following optimal control problem and solving it via direct
 153 collocation:

$$154 \quad \underset{\mathbf{x}(t), \mathbf{u}(t)}{\text{minimize}} \quad J(\mathbf{z}(t), \mathbf{z}'(t), \mathbf{u}(t))$$

$$155 \quad \text{subject to} \quad \mathbf{z}' = f(\mathbf{z}, \mathbf{u})$$

$$156 \quad \mathbf{x}_L \leq \mathbf{x} \leq \mathbf{x}_U$$

$$157 \quad \mathbf{u}_L \leq \mathbf{u} \leq \mathbf{u}_U$$

158 The cost functional $J(\mathbf{z}(t), \mathbf{z}'(t), \mathbf{u}(t))$ is minimized with respect to a bounded state and control
 159 and a constraint on the first derivative of the state vector from the explicit form of the equations of
 160 motion. The cost functional includes a tracking term for both the keypoints and the inertial data,
 161 J_{track} , as well as an effort term for both the joint torque actuators and the residual forces, J_{effort} :

$$162 \quad J = J_{track} + J_{effort};$$

$$163 \quad J_{track} = \sum_{i=1}^{n_{keypoint}} \left[(x_i^{keypoint} - x_i^{state})^2 + (y_i^{keypoint} - y_i^{state})^2 \right] \dots$$

$$164 \quad + \sum_{j=1}^{n_{IMU}} \left[(\ddot{x}_j^{IMU} - \ddot{x}_j^{state})^2 + (\ddot{y}_j^{IMU} - \ddot{y}_j^{state})^2 + (\omega_j^{IMU} - \omega_j^{state})^2 \right];$$

$$165 \quad J_{effort} = \sum_{m=1}^{n_{torques}} (T_k)^2 + \sum_{n=1}^{n_{residuals}} (R_n)^2$$

166 We transcribed the large-scale, sparse nonlinear optimization problem via direct collocation using
167 the OptimTraj library for MATLAB (Kelly, 2017).

168

169 *2.5 Kinematics Estimation: IMU-Only*

170 To perform dynamic optimization with IMU data alone, we took the same steps as in the
171 dynamically constrained fusion approach (2.4) but removed the keypoint terms from within the
172 J_{track} portion of the cost. We followed a previously proposed method and applied the assumption
173 that motion was periodic to overcome the drift resulting from integrating noisy IMU data (Dorschky
174 et al., 2019). This involved segmenting the walking data into individual gait cycles and using the
175 mean gait cycle as the input to the J_{track} term.

176

177 *2.6 Kinematics Estimation: Unconstrained Fusion*

178 For fusion of IMU and video data via unconstrained optimization, we formulated a simplified
179 optimization problem where J_{track} from the IMU and vision optimization was minimized, excluding
180 J_{effort} and constraints on system dynamics and model controls (Halilaj et al., 2021). Here, the
181 optimal set of kinematics was determined by minimizing the error between the experimental IMU
182 and video data and the synthetic IMU and keypoint profiles projected from the subject's current
183 state.

184

185 *2.7 Synthetic Data Generation*

186 In addition to building simulations with the experimentally captured data, we generated synthetic
187 data to investigate how each of the four approaches responded to changes in noise magnitude.
188 We first estimated the naturally occurring noise background, φ , from the experimental data.
189 Ground truth trajectories for each joint center's position and each body segment's accelerations
190 and angular velocities were calculated via marker-based motion capture data and analytic

191 equations formed in Autolev, as noted above. Noise was defined as the difference between the
192 ground-truth trajectories and IMU-based (angular velocity and linear acceleration) or video-based
193 (joint center position) trajectories. We multiplied this experimental noise background by a
194 scale factor, S , to achieve synthetic data with new noise magnitudes, without editing the shape
195 of the experimentally observed noise distribution:

$$196 \quad \varphi = data^{exp} - data^{mocap}$$

$$197 \quad data^{synth} = S\varphi + data^{mocap}$$

198

199 Using marker-based motion capture as the ground truth, the mean \pm standard deviation keypoint
200 root-mean-square error (RMSE) for the five subjects was 3.5 ± 0.2 cm. We scaled the naturally
201 occurring noise background, φ , for each subject to RMSEs of 6.0, 3.5, and 1.0 cm by adjusting
202 only the scale of the noise background while maintaining its original distribution. These new noise
203 background magnitudes represented low, medium, and high accuracy conditions, based on
204 single-view and multi-view approaches (Iskakov et al., 2019; Kadkhodamohammadi & Padoy,
205 2019; Kanazawa et al., 2018; Kocabas et al., 2020). An RMSE of 6.0 cm corresponds to single-
206 view approaches such as the Human Mesh Recovery (HMR) (Kanazawa et al., 2018) and Video
207 Inference for Body Pose And Shape Estimation (VIBE) (Kocabas et al., 2020). An RMSE of 3.5
208 cm corresponds to multi-camera algebraic triangulation approaches like what was used in this
209 study. An RMSE of 1.0 cm corresponds to multi-camera methods incorporating learnable
210 triangulation (Iskakov et al., 2019; Kadkhodamohammadi & Padoy, 2019). The IMU data had a
211 mean \pm standard deviation signal-to-noise ratio (SNR) of 13.2 ± 0.4 dB.

212

213 To generate the IMU synthetic data, we scaled the naturally occurring noise background for each
214 subject to SNRs of 10, 17.5, and 25 dB, which represented low, medium, and high IMU accuracy
215 conditions. These conditions corresponded to IMU data influenced by electrical noise in the form

216 of white noise, scale factor noise, and bias noise (Park & Gao, 2008), a range of commonly
217 occurring static misplacement and misorientation errors (Tan et al., 2019), and a range of
218 previously established soft-tissue motion magnitudes naturally occurring during walking
219 (Fiorentino et al., 2017). To determine appropriate magnitudes to which the experimental IMU
220 noise backgrounds would be scaled, we simulated combinations of misplacement, misorientation,
221 and soft-tissue motion artifacts by formulating analytic equations for each body segment's
222 accelerations and angular velocity in Autolev:

$$223 \mathbf{a}_x, \mathbf{a}_y, \boldsymbol{\omega}_z = f(\mathbf{q}, e_{\text{misplace}}, e_{\text{misalign}}, e_{\text{tissue}})$$

$$224 e_{\text{tissue}} \sim \mathcal{N}(\mu, \sigma^2)$$

225 We added error terms while deriving the body segment inertial profiles to model the static
226 misplacement, e_{misplace} , the static misalignment, e_{misalign} , and the variable misplacement due to
227 soft-tissue motion, e_{tissue} . We calculated the noise background magnitudes corresponding to
228 these errors as the difference between the inertial profiles of the body segments derived with and
229 without incorporating the sources of error, and then scaled the error terms to represent the range
230 of expected naturally occurring noise magnitudes (Table 2). We sampled e_{tissue} from a normal
231 distribution with μ and σ equivalent to the mean and standard deviation of soft-tissue motion
232 magnitudes measured through X-rays (Fiorentino et al., 2017).

233

234 *2.8 Performance Evaluation*

235 We computed mean-per-joint position error and joint angle error between the simulation results
236 and ground truth marker-based motion capture data for each optimization approach and noise
237 profile. We used a one-way repeated measures analysis of variance (RM-ANOVA) and Tukey's
238 Honest Significant Difference (HSD) for post-hoc analysis to test the leading hypothesis that
239 dynamically constrained fusion would result in lower kinematic errors compared to the other three
240 approaches. The test was carried out for two primary kinematic outcomes: the mean full-body

241 RMSEs for joint angles and joint center positions. A two-way RM-ANOVA followed by an HSD
242 test within noise conditions were used to test the second hypothesis that dynamically constrained
243 fusion would outperform the other three methods when the data were characterized by different
244 noise profiles. The two-way RM-ANOVA considered both the four competing methods and the
245 nine repeated combinations of IMU and video data noise profiles. Results are presented as mean
246 \pm standard deviation of the per-joint RMSE compared to marker-based motion capture. An
247 Anderson-Darling test for normality was used to confirm that the data were normally distributed
248 (Yap & Sim, 2011).

249

250

3. RESULTS

251 *3.1 Comparison of Modeling Approaches*

252 Dynamically constrained fusion performed better than single-modality methods, but similarly to
253 unconstrained fusion when using the experimental data (Fig. 2b; Fig. 3). It improved estimation
254 of joint angles by $6.0^\circ \pm 1.2^\circ$ ($p < 0.0001$) over the vision-only approach and joint centers by 4.5
255 ± 2.8 cm ($p = 0.0018$) over the IMU-only approach. Joint angle estimates with the vision-only
256 approach were the least accurate of the four approaches, with RMSEs of $5.1^\circ \pm 1.7^\circ$ at the hip,
257 $9.7^\circ \pm 3.2^\circ$ at the knee, and $16.0^\circ \pm 1.2^\circ$ at the ankle. Similarly, joint center position estimates with
258 the IMU-only approach were the least accurate of the four approaches, producing errors ranging
259 from 5.6 ± 2.4 cm at the hip to 6.8 ± 3.3 cm at the ankle. The two fusion approaches performed
260 similarly to each other and better than single modality approaches by maintaining accuracy with
261 respect to both joint angles and joint positions. However, dynamically constrained fusion did
262 facilitate improvements over unconstrained fusion in estimates of the ankle angle by $3.3^\circ \pm 1.3^\circ$
263 ($p = 0.0076$).

264

265 *3.2 Sensitivity to Noise*

266 Dynamically constrained fusion performed better than unconstrained fusion when the accuracy of
267 IMU data was low and the accuracy of the video data was high, whereas unconstrained fusion
268 performed better in the opposite scenario (Fig. 4). When the IMU data were of low quality (SNR
269 of 10 dB) and the predicted keypoints from video data were of high quality (RMSE of 1.0 cm),
270 constrained fusion improved estimates of joint angles by RMSEs of $3.7^\circ \pm 1.2^\circ$ ($p < 0.0001$) and
271 joint centers by 1.9 ± 0.5 cm ($p < 0.0001$) over unconstrained fusion. When the IMU data were of
272 high quality (SNR of 25 dB) and the predicted keypoints were of low quality (RMSE of 6.0 cm),
273 unconstrained fusion improved estimates of joint angles by $3.0^\circ \pm 1.4^\circ$ ($p = 0.0049$) and joint
274 center positions by 1.2 ± 0.7 cm ($p = 0.0183$) over constrained fusion. However, when the quality
275 of IMU data and predicted keypoints was scaled up and down simultaneously, differences
276 between the fusion techniques were not significant.

277
278 Single-modality approaches generally performed worse than fusion approaches across the varied
279 data qualities, with some exceptions (Fig. 5). The vision-only approach resulted in significantly
280 worse joint angle estimates than the fusion approaches at every condition except when very low
281 IMU data quality (SNR of 10 dB) was paired with very high keypoint data quality (RMSE of 1 cm).
282 At this condition, vision-only matched constrained fusion ($p = 0.8071$) with a joint angle RMSE of
283 $3.3^\circ \pm 0.5^\circ$. The IMU-only approach resulted in significantly worse joint center position estimates
284 compared to the fusion approaches at five out of the nine conditions. At combinations of medium
285 to excellent IMU data accuracy (17.5 – 25 dB) and poor to medium keypoint data accuracy (6.0 –
286 3.5 cm), the IMU-only approach performed equivalently to fusion methods.

287

288 4. DISCUSSION

289 The complementary strengths of wearable sensing, computer vision, and biomechanical modeling
290 could enhance our ability to capture motion and study gait with greater flexibility and cost-
291 effectiveness than current marker-based approaches. Here, we proposed to fuse video and

292 inertial data with a biomechanical model that simultaneously tracks video and IMU data and
293 investigated when this method improves estimation of kinematics over single-modality methods
294 and unconstrained fusion. We found that fusion of video and inertial data improves kinematics
295 over single-modality methods by achieving high accuracy for both joint angles and joint center
296 positions across all the tested video and IMU noise backgrounds. We also found that dynamically
297 constrained fusion with a biomechanical model is advantageous over unconstrained fusion when
298 the quality of inertial sensing data is low and the quality of computer vision models is high,
299 whereas unconstrained fusion is advantageous in the opposite case. When the inertial and vision
300 data noise is equally low or equally high, both types of fusion work equally well, but unconstrained
301 is more computationally efficient.

302

303 When interpreting these findings, it is important to consider some of the study's limitations.
304 Biomechanical modeling simplifications—reducing degrees of freedom, modeling the head, arms,
305 and torso as a single rigid body, and connecting bones to joints by their end points—can affect
306 the results of simulations. Yet, this simplified approach provides baseline insight on how physics-
307 based modeling can contribute to improvement of IMU-video fusion. We expect that models with
308 greater complexities and constraints, like OpenSim, will amplify but not overturn the conclusions
309 drawn here. Furthermore, we created synthetic data for testing each approach across different
310 noise magnitudes by simply scaling the noise backgrounds inherent to the experimental IMU and
311 video data. We find this approach elegant and the assumption that the noise distribution remains
312 constant across noise magnitudes more reasonable than making assumptions about that
313 distribution (e.g., Gaussian, uniform, etc.), but a validation of the synthetically scaled noise profiles
314 could be used to test that hypothesis in the future. A final limitation is that only walking was
315 considered here. It remains to be determined if the reported findings hold across other activities.

316

317 The finding that fusion of video and IMU data is advantageous to single-modality approaches is
318 consistent with findings from other disciplines, despite the lack of exploration in biomechanics.
319 State estimation and simultaneous localization and mapping (SLAM) in autonomous robot
320 navigation is commonly achieved by fusing IMU and video data with extended Kalman filters (R.
321 Smith et al., 1990) and modified particle filters (Montemerlo et al., 2002). Currently, this fusion
322 method provides the most viable alternative to GPS and lidar-based odometry in aerial navigation
323 (Scaramuzza & Zhang, 2020). IMUs overcome visual SLAM limitations like occlusion, motion blur,
324 a lack of visible textures, and inaccurate velocity and acceleration estimates, while videos help
325 enable IMU recalibration in real-time to overcome drift (Mirzaei & Roumeliotis, 2008; Nikolic et al.,
326 2014). The complementary nature of videos and IMUs explains why fusion methods consistently
327 outperformed single-modality methods across the entire range of tested noise conditions and why
328 they should be adopted in biomechanics as they are in robot-state estimation. However, while
329 fusion is generally better, attention must be paid to both data quality and computational cost to
330 select the most appropriate fusion approach for a particular application.

331
332 The overlap between biomechanical models and IMUs causes the unconstrained and
333 biomechanically constrained fusion approaches to diverge under specific noise conditions.
334 Biomechanical models provide mathematical expressions relating applied forces to rigid-body
335 accelerations and velocities. IMUs provide experimental measurements of rigid-body
336 accelerations and angular velocities. When IMU data are inaccurate, adding a model is beneficial
337 because the underlying optimizer can leverage the model's physics information and reduce its
338 dependence on the suboptimal IMU data. However, when the IMU data are more accurate than
339 the model, given modeling simplifications, adding the model becomes detrimental. Because IMU
340 data quality is limited by miscalibration errors and soft-tissue artifacts, the incorporation of a
341 biomechanical model will likely remain beneficial for natural environment applications of fusion

342 methods. Furthermore, incorporation of a model is likely to benefit measurements of faster
343 activities associated with larger skin deformations.

344

345 As the prevalence of health monitoring in natural environments increases, so will the frequency
346 with which patients and clinicians are charged with setting up lightweight and portable health-
347 monitoring systems. Markerless motion capture methods must therefore be robust to the IMU and
348 camera miscalibrations resulting from suboptimal setups by nonexperts. Since fusion of
349 complementary modalities has proven to be more robust to noisy data than single modality
350 methods, we recommend that greater emphasis is placed on thoroughly exploring and
351 benchmarking data fusion approaches for biomechanical applications. Our work provides a
352 preliminary comparison of emerging techniques that could make motion capture more accessible.
353 Our findings could help researchers and clinicians make more informed decisions, weighing the
354 required accuracy for a given application against sensor density and computational complexity.
355 Our published code provides an opportunity to further verify our conclusions with real video and
356 IMU data from different laboratories.

357 **Acknowledgements:**

358 Research reported in this publication was supported by the United States National Science
359 Foundation (NSF) Graduate Research Fellowship Program (award numbers DGE1745016 and
360 DGE2140739), a Korean Government Fellowship, and the NSF Disability and Rehabilitation
361 Engineering program (award number CBET 2145473).

362

363 **Data Availability:**

364 All the code required to generate the findings of this study is made available via GitHub:

365 <https://github.com/CMU-MBL/IMUVisionBiomechanics.git>

366

367 **Conflict of Interest Statement:**

368 The authors declare no competing interests.

369

References

- 370 Al Borno, M., O'Day, J., Ibarra, V., Dunne, J., Seth, A., Habib, A., Ong, C., Hicks, J., Uhrich, S.,
371 & Delp, S. (2022). OpenSense: An open-source toolbox for inertial-measurement-unit-
372 based measurement of lower extremity kinematics over long durations. *Journal of*
373 *NeuroEngineering and Rehabilitation*, 19(1), 22. [https://doi.org/10.1186/s12984-022-](https://doi.org/10.1186/s12984-022-01001-x)
374 01001-x
- 375 Bloesch, M., Burri, M., Sommer, H., Siegwart, R., & Hutter, M. (2018). The Two-State Implicit
376 Filter Recursive Estimation for Mobile Robots. *IEEE Robotics and Automation Letters*,
377 3(1), 573–580. <https://doi.org/10.1109/LRA.2017.2776340>
- 378 Bloesch, M., Gehring, C., Fankhauser, P., Hutter, M., Hoepflinger, M. A., & Siegwart, R. (2013).
379 State estimation for legged robots on unstable and slippery terrain. *2013 IEEE/RSJ*
380 *International Conference on Intelligent Robots and Systems*, 6058–6064.
381 <https://doi.org/10.1109/IROS.2013.6697236>
- 382 Chen, Y., Wang, Z., Peng, Y., Zhang, Z., Yu, G., & Sun, J. (2018). Cascaded Pyramid Network
383 for Multi-Person Pose Estimation. *ArXiv:1711.07319 [Cs]*.
384 <http://arxiv.org/abs/1711.07319>
- 385 de Vries, W. H. K., Veeger, H. E. J., Baten, C. T. M., & van der Helm, F. C. T. (2009). Magnetic
386 distortion in motion labs, implications for validating inertial magnetic sensors. *Gait &*
387 *Posture*, 29(4), 535–541. <https://doi.org/10.1016/j.gaitpost.2008.12.004>
- 388 Delp, S. L., Anderson, F. C., Arnold, A. S., Loan, P., Habib, A., John, C. T., Guendelman, E., &
389 Thelen, D. G. (2007). OpenSim: Open-Source Software to Create and Analyze Dynamic
390 Simulations of Movement. *IEEE Transactions on Biomedical Engineering*, 54(11), 1940–
391 1950. <https://doi.org/10.1109/TBME.2007.901024>
- 392 Delp, S. L., Loan, J. P., Hoy, M. G., Zajac, F. E., Topp, E. L., & Rosen, J. M. (1990). An
393 interactive graphics-based model of the lower extremity to study orthopaedic surgical

- 394 procedures. *IEEE Transactions on Biomedical Engineering*, 37(8), 757–767.
395 <https://doi.org/10.1109/10.102791>
- 396 Dorschky, E., Nitschke, M., Seifer, A.-K., van den Bogert, A. J., & Eskofier, B. M. (2019).
397 Estimation of gait kinematics and kinetics from inertial sensor data using optimal control
398 of musculoskeletal models. *Journal of Biomechanics*, 95, 109278.
399 <https://doi.org/10.1016/j.jbiomech.2019.07.022>
- 400 Fiorentino, N. M., Atkins, P. R., Kutschke, M. J., Goebel, J. M., Foreman, K. B., & Anderson, A.
401 E. (2017). Soft tissue artifact causes significant errors in the calculation of joint angles
402 and range of motion at the hip. *Gait & Posture*, 55, 184–190.
403 <https://doi.org/10.1016/j.gaitpost.2017.03.033>
- 404 Halilaj, E., Shin, S., Rapp, E., & Xiang, D. (2021). American Society of Biomechanics Early
405 Career Achievement Award 2020: Toward Portable and Modular Biomechanics Labs:
406 How Video and IMU Fusion Will Change Gait Analysis. *Journal of Biomechanics*,
407 110650. <https://doi.org/10.1016/j.jbiomech.2021.110650>
- 408 Hartley, R. I., & Sturm, P. (1997). Triangulation. *Computer Vision and Image Understanding*,
409 68(2), 146–157. <https://doi.org/10.1006/cviu.1997.0547>
- 410 Huang, Y., Kaufmann, M., Aksan, E., Black, M. J., Hilliges, O., & Pons-Moll, G. (2018). Deep
411 inertial poser: Learning to reconstruct human pose from sparse inertial measurements in
412 real time. *ACM Transactions on Graphics*, 37(6), 1–15.
413 <https://doi.org/10.1145/3272127.3275108>
- 414 Iskakov, K., Burkov, E., Lempitsky, V., & Malkov, Y. (2019). Learnable Triangulation of Human
415 Pose. *ArXiv:1905.05754 [Cs]*. <http://arxiv.org/abs/1905.05754>
- 416 Joo, H., Simon, T., Li, X., Liu, H., Tan, L., Gui, L., Banerjee, S., Godisart, T., Nabbe, B.,
417 Matthews, I., Kanade, T., Nobuhara, S., & Sheikh, Y. (2019). Panoptic Studio: A
418 Massively Multiview System for Social Interaction Capture. *IEEE Transactions on*

- 419 *Pattern Analysis and Machine Intelligence*, 41(1), 190–204.
- 420 <https://doi.org/10.1109/TPAMI.2017.2782743>
- 421 Kadkhodamohammadi, A., & Padoy, N. (2019). *A generalizable approach for multi-view 3D*
- 422 *human pose regression* (arXiv:1804.10462). arXiv. <http://arxiv.org/abs/1804.10462>
- 423 Kanazawa, A., Black, M. J., Jacobs, D. W., & Malik, J. (2018). End-to-end Recovery of Human
- 424 Shape and Pose. *ArXiv:1712.06584 [Cs]*. <http://arxiv.org/abs/1712.06584>
- 425 Kanko, R. M., Laende, E. K., Davis, E. M., Selbie, W. S., & Deluzio, K. J. (2021). Concurrent
- 426 assessment of gait kinematics using marker-based and markerless motion capture.
- 427 *Journal of Biomechanics*, 127, 110665. <https://doi.org/10.1016/j.jbiomech.2021.110665>
- 428 Karatsidis, A., Bellusci, G., Schepers, H., de Zee, M., Andersen, M., & Veltink, P. (2016).
- 429 Estimation of Ground Reaction Forces and Moments During Gait Using Only Inertial
- 430 Motion Capture. *Sensors*, 17(12), 75. <https://doi.org/10.3390/s17010075>
- 431 Karatsidis, A., Jung, M., Schepers, H. M., Bellusci, G., de Zee, M., Veltink, P. H., & Andersen,
- 432 M. S. (2018). Predicting kinetics using musculoskeletal modeling and inertial motion
- 433 capture. *ArXiv:1801.01668 [Physics]*. <http://arxiv.org/abs/1801.01668>
- 434 Karatsidis, A., Jung, M., Schepers, H. M., Bellusci, G., de Zee, M., Veltink, P. H., & Andersen,
- 435 M. S. (2019). Musculoskeletal model-based inverse dynamic analysis under ambulatory
- 436 conditions using inertial motion capture. *Medical Engineering & Physics*, 65, 68–77.
- 437 <https://doi.org/10.1016/j.medengphy.2018.12.021>
- 438 Kelly, M. (2017). An Introduction to Trajectory Optimization: How to Do Your Own Direct
- 439 Collocation. *SIAM Review*, 59(4), 849–904. <https://doi.org/10.1137/16M1062569>
- 440 Kocabas, M., Athanasiou, N., & Black, M. J. (2020). VIBE: Video Inference for Human Body
- 441 Pose and Shape Estimation. *ArXiv:1912.05656 [Cs]*. <http://arxiv.org/abs/1912.05656>
- 442 Madgwick, S. O. H. (2010). *An efficient orientation filter for inertial and inertial/magnetic sensor*
- 443 *arrays*. 32.

- 444 Mahony, R., Hamel, T., & Pflimlin, J.-M. (2008). Nonlinear Complementary Filters on the Special
445 Orthogonal Group. *IEEE Transactions on Automatic Control*, 53(5), 1203–1218.
446 <https://doi.org/10.1109/TAC.2008.923738>
- 447 Marra, C., Chen, J. L., Coravos, A., & Stern, A. D. (2020). Quantifying the use of connected
448 digital products in clinical research. *Npj Digital Medicine*, 3(1), 50.
449 <https://doi.org/10.1038/s41746-020-0259-x>
- 450 Mirzaei, F. M., & Roumeliotis, S. I. (2008). A Kalman Filter-Based Algorithm for IMU-Camera
451 Calibration: Observability Analysis and Performance Evaluation. *IEEE Transactions on*
452 *Robotics*, 24(5), 1143–1156. <https://doi.org/10.1109/TRO.2008.2004486>
- 453 Montemerlo, M., Thrun, S., Koller, D., & Wegbreit, B. (2002). FastSLAM: A Factored Solution to
454 the Simultaneous Localization and Mapping Problem. *AAAI-02 Proceedings*, 6.
- 455 Mundt, M., Johnson, W. R., Potthast, W., Markert, B., Mian, A., & Alderson, J. (2021). A
456 Comparison of Three Neural Network Approaches for Estimating Joint Angles and
457 Moments from Inertial Measurement Units. *Sensors*, 21(13), 4535.
458 <https://doi.org/10.3390/s21134535>
- 459 Mundt, M., Thomsen, W., Witter, T., Koeppe, A., David, S., Bamer, F., Potthast, W., & Markert,
460 B. (2020). Prediction of lower limb joint angles and moments during gait using artificial
461 neural networks. *Medical & Biological Engineering & Computing*, 58(1), 211–225.
462 <https://doi.org/10.1007/s11517-019-02061-3>
- 463 Nikolic, J., Rehder, J., Burri, M., Gohl, P., Leutenegger, S., Furgale, P. T., & Siegwart, R.
464 (2014). A synchronized visual-inertial sensor system with FPGA pre-processing for
465 accurate real-time SLAM. *2014 IEEE International Conference on Robotics and*
466 *Automation (ICRA)*, 431–437. <https://doi.org/10.1109/ICRA.2014.6906892>
- 467 Park, M., & Gao, Y. (2008). Error and Performance Analysis of MEMS-based Inertial Sensors
468 with a Low-cost GPS Receiver. *Sensors*, 8(4), 2240–2261.
469 <https://doi.org/10.3390/s8042240>

- 470 Petersen, A., & Koch, R. (2012). *Video-based realtime IMU-camera calibration for robot*
471 *navigation* (N. Kehtarnavaz & M. F. Carlsohn, Eds.; p. 843706).
472 <https://doi.org/10.1117/12.924066>
- 473 Picerno, P. (2017). 25 years of lower limb joint kinematics by using inertial and magnetic
474 sensors: A review of methodological approaches. *Gait & Posture*, *51*, 239–246.
475 <https://doi.org/10.1016/j.gaitpost.2016.11.008>
- 476 R. Smith, M. Self, & P. Cheeseman. (1990). Estimating uncertain spatial relationships in
477 robotics. *Autonomous Robot Vehicles*.
- 478 Rapp, E., Shin, S., Thomsen, W., Ferber, R., & Halilaj, E. (2021). Estimation of kinematics from
479 inertial measurement units using a combined deep learning and optimization framework.
480 *Journal of Biomechanics*, *116*, 110229. <https://doi.org/10.1016/j.jbiomech.2021.110229>
- 481 Roetenberg, D., Luinge, H., & Slycke, P. (2013). *Xsens MVN: Full 6DOF Human Motion*
482 *Tracking Using Miniature Inertial Sensors*. 10.
- 483 Sabatini, A. M. (2011). Estimating Three-Dimensional Orientation of Human Body Parts by
484 Inertial/Magnetic Sensing. *Sensors*, *11*(2), 1489–1525.
485 <https://doi.org/10.3390/s110201489>
- 486 Scaramuzza, D., & Zhang, Z. (2020). Aerial Robots, Visual-Inertial Odometry of. In M. H. Ang,
487 O. Khatib, & B. Siciliano (Eds.), *Encyclopedia of Robotics* (pp. 1–9). Springer Berlin
488 Heidelberg. https://doi.org/10.1007/978-3-642-41610-1_71-1
- 489 Seethapathi, N., Wang, S., Saluja, R., Blohm, G., & Kording, K. P. (2019). *Movement science*
490 *needs different pose tracking algorithms* (arXiv:1907.10226). arXiv.
491 <http://arxiv.org/abs/1907.10226>
- 492 Strutzenberger, G., Kanko, R., Selbie, S., Schwameder, H., & Deluzio, K. (2021).
493 *ASSESSMENT OF KINEMATIC CMJ DATA USING A DEEP LEARNING ALGORITHM-*
494 *BASED MARKERLESS MOTION CAPTURE SYSTEM*. 4.

- 495 Tan, T., Chiasson, D. P., Hu, H., & Shull, P. B. (2019). Influence of IMU position and orientation
496 placement errors on ground reaction force estimation. *Journal of Biomechanics*, *97*,
497 109416. <https://doi.org/10.1016/j.jbiomech.2019.109416>
- 498 Trumble, M., Gilbert, A., Malleson, C., Hilton, A., & Collomosse, J. (2017). Total Capture: 3D
499 Human Pose Estimation Fusing Video and Inertial Sensors. *Proceedings of the British*
500 *Machine Vision Conference 2017*, 14. <https://doi.org/10.5244/C.31.14>
- 501 Uhlrich, S. D., Falisse, A., Kidziński, Ł., Muccini, J., Ko, M., Chaudhari, A. S., Hicks, J. L., &
502 Delp, S. L. (2022). *OpenCap: 3D human movement dynamics from smartphone videos*
503 [Preprint]. Bioengineering. <https://doi.org/10.1101/2022.07.07.499061>
- 504 Yap, B. W., & Sim, C. H. (2011). Comparisons of various types of normality tests. *Journal of*
505 *Statistical Computation and Simulation*, *81*(12), 2141–2155.
506 <https://doi.org/10.1080/00949655.2010.520163>
- 507 Yi, X., Zhou, Y., Golyanik, V., Habermann, M., Shimada, S., Theobalt, C., & Xu, F. (n.d.).
508 *Physical Inertial Poser (PIP): Physics-aware Real-time Human Motion Tracking from*
509 *Sparse Inertial Sensors*. 15.
- 510 Yi, X., Zhou, Y., & Xu, F. (2021). *TransPose: Real-time 3D Human Translation and Pose*
511 *Estimation with Six Inertial Sensors* (arXiv:2105.04605). arXiv.
512 <http://arxiv.org/abs/2105.04605>
- 513

TABLES

Table 1. Qualitative comparison of state-of-the-art IMU and video-based motion capture techniques for measuring joint kinematics.

Modality	Method	Example Articles	Advantages	Disadvantages
IMUs	Sensor-fusion Filters (e.g., EKF, Madgwick, Mahoney)	Mahony, 2008. Madgwick, 2010. Sabatini, 2011. Joukov, 2014. Al Borno, 2022.	Computationally efficient; Open source	Magnetometers are often unreliable Magnetometer-free approaches are inaccurate
	Deep Learning (e.g., CNNs, LSTMs, Transformers)	Huang, 2018. Rapp, 2021. Yi, 2021-22. Mundt, 2020-2021.	Implicitly learns noise; Open source	Training data are not sufficiently representative of pathologies and activities
	Biomechanical Modeling: Static Optimization	Roetenberg, 2013. Karatsidis, 2016-19.	Predicts GRFs, muscle forces, and joint reaction forces	Requires drift correction using additional sensors; Computational cost; Closed source
	Biomechanical Modeling: Direct Collocation	Dorschky, 2019.	Predicts GRFs, muscle forces, and joint reaction forces	Requires drift correction using limiting assumptions; Computational cost; Closed source
Videos	Deep learning & Unconstrained Optimization	Kanazawa, 2018. Iskakov, 2019. Zhang, 2020. Kocabas, 2020-21.	Computationally efficient; Open source	Data-driven: training data not representative of clinical populations; Sensitive to occlusions
	Deep Learning & Biomechanical Modeling	Kanko, 2021. Strutzenberger, 2021. Uhlrich, 2022.	Predicts GRFs, muscle forces, and joint reaction forces; Open source	Data-driven: training data not representative of clinical populations; Computational cost
IMUs & Videos	Deep learning & Unconstrained Optimization	Halilaj, 2021.	Computationally efficient; Merges complementary modalities; No integration of inertial data necessary	Poor initial estimations from video are propagated in the optimization
	Deep learning & Dynamically Constrained Optimization	Proposed Method	Predicts GRFs, muscle forces, and joint reaction forces; Merges complementary modalities while satisfying the laws of physics No integration of inertial data necessary; Accurate with noisy IMU data	Currently, 2-D proof of concept with 3-D validity remaining to be tested; Computational cost

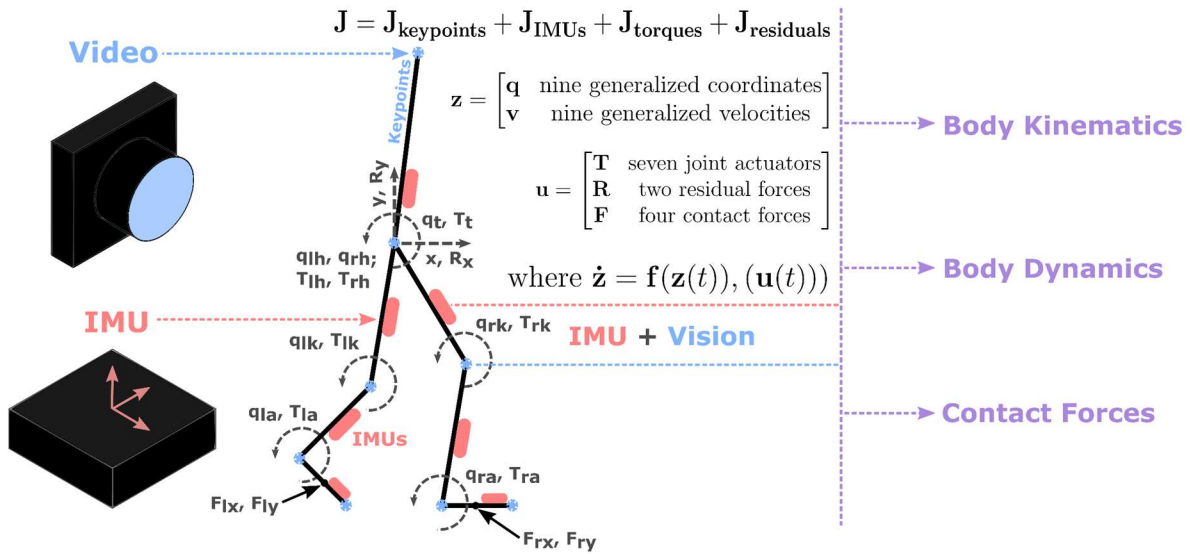
Table 2. Sources of uncertainty for each modeled IMU signal-to-noise ratio (SNR) profile.

Misplacement (cm)	Misalignment (deg)	Soft-Tissue Motion (cm)	IMU SNR (dB)
0.5	1	0.5	26.7
2.5	5	1.0	17.7
5.0	10	5.0	10.1

516

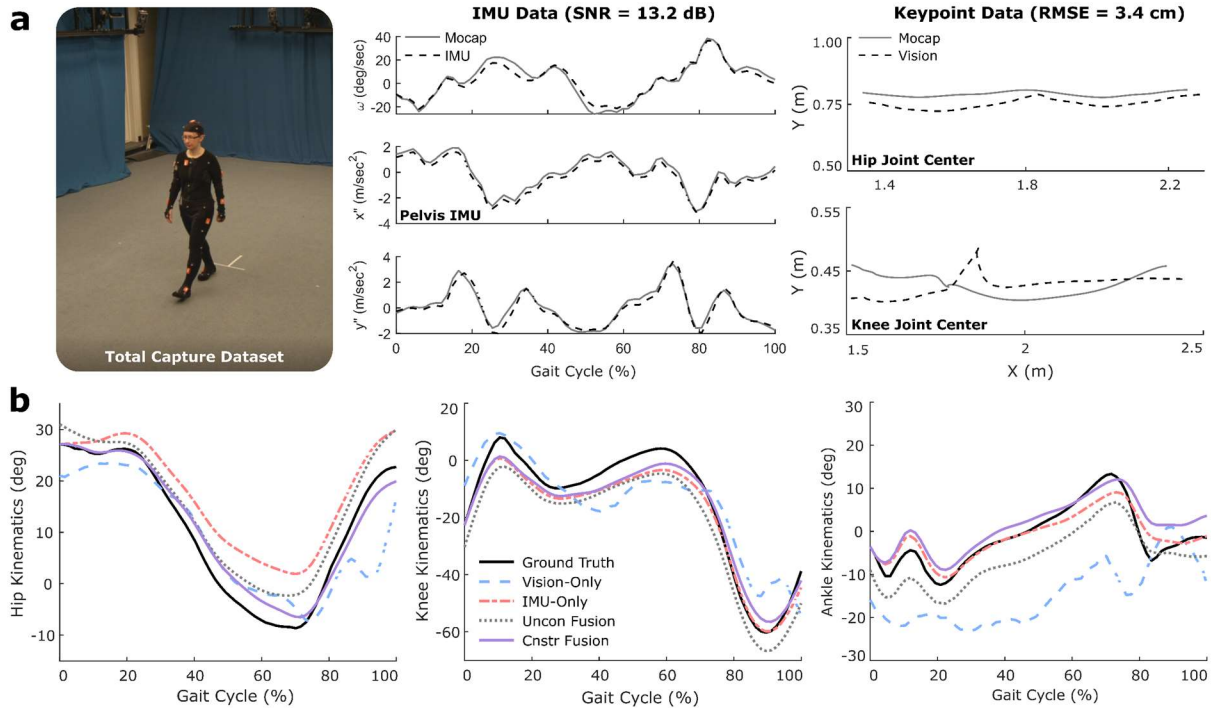
517

FIGURES



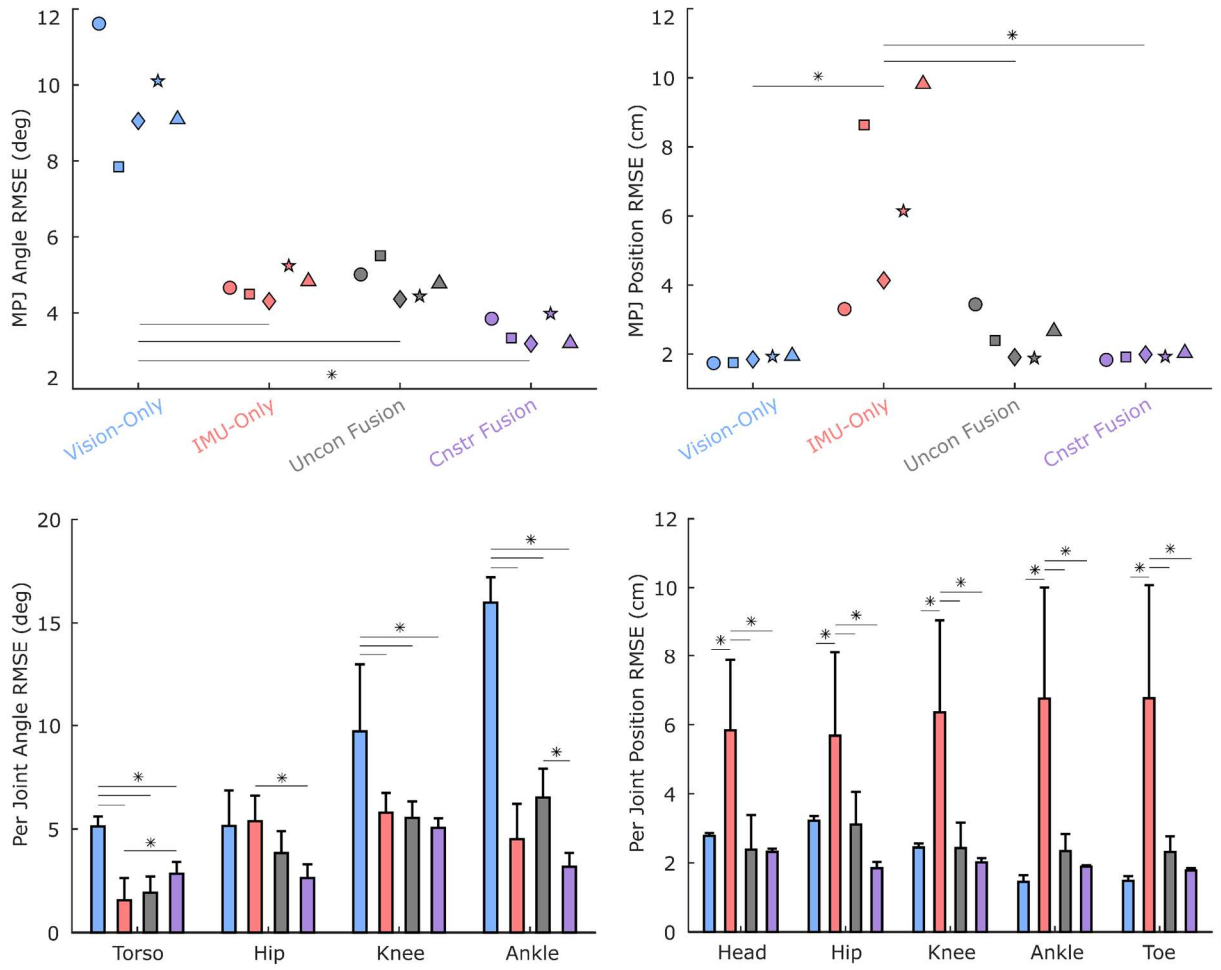
518

519 **Fig. 1. Biomechanical Model and Dynamics Overview.** Video and inertial measurement unit (IMU) data are fused
 520 into a single optimal control trajectory tracking problem, where the state of a planar musculoskeletal model is optimized
 521 to produce joint center trajectories and inertial profiles that match the experimental data. A nine degree-of-freedom (two
 522 translational, seven rotational) model is actuated by seven joint torques, four ground contact forces, and two residual
 523 forces accounting for dynamic inconsistencies due to modeling simplifications. The model fuses data from eight
 524 anatomical keypoints acquired from three-dimensional triangulation of video data and seven inertial measurement units
 525 placed on each rigid body segment. Direct collocation is used to minimize a cost functional with keypoint and IMU
 526 tracking error costs and an effort cost for regulating the joint torques and residual forces.



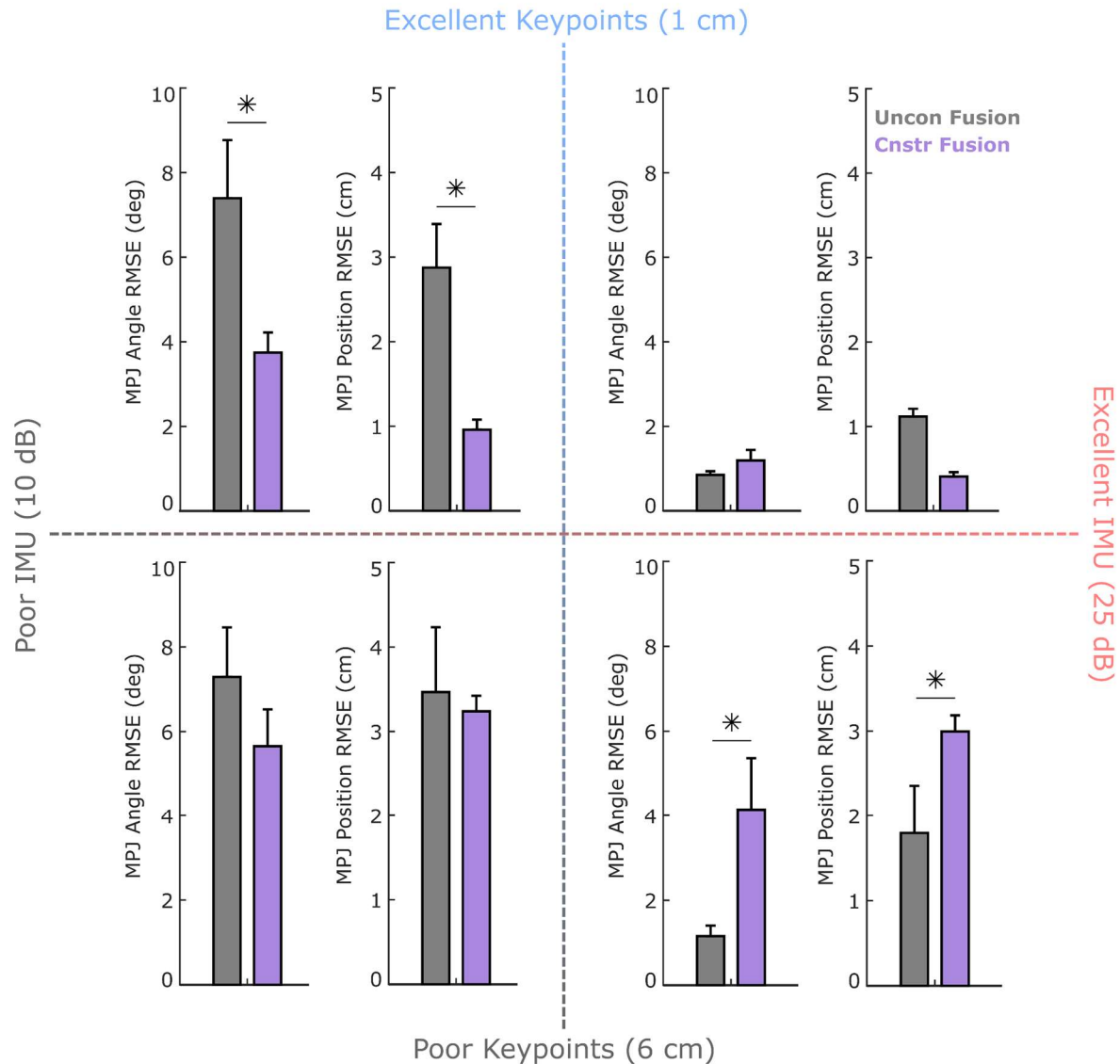
527

528 **Fig. 2. Experimental Data and Resulting Markerless Kinematics. (a)** Total Capture is a public dataset of five
529 subjects performing different activities, while recorded with marker-based motion capture, inertial measurement units
530 (IMU), and four videos. Only the walking trials were analyzed here. The IMU data had a signal-to-noise (SNR) ratio of
531 13.2 dB, while the video-based keypoints (i.e., joint center estimations) had a root-mean-squared error (RMSE) of 3.4
532 cm. **(b)** Dynamically constrained fusion of IMU and video data via a biomechanical model and direct collocation (Cnstr
533 Fusion, in solid magenta) improved kinematic predictions over competing markerless motion capture approaches
534 (shown for a single female subject). Each approach was tested on all subjects in the Total Capture Dataset after
535 calibrating IMU data, triangulating video data into 3D keypoints, and projecting 3D data into each subject's sagittal
536 plane. Noise levels of IMU and keypoint data were calculated with respect to marker-based motion capture as the
537 ground truth. Constrained fusion outperformed both single modality approaches and unconstrained fusion (Uncon
538 Fusion, in dashed gray) across the hip, knee, and ankle joint angles.



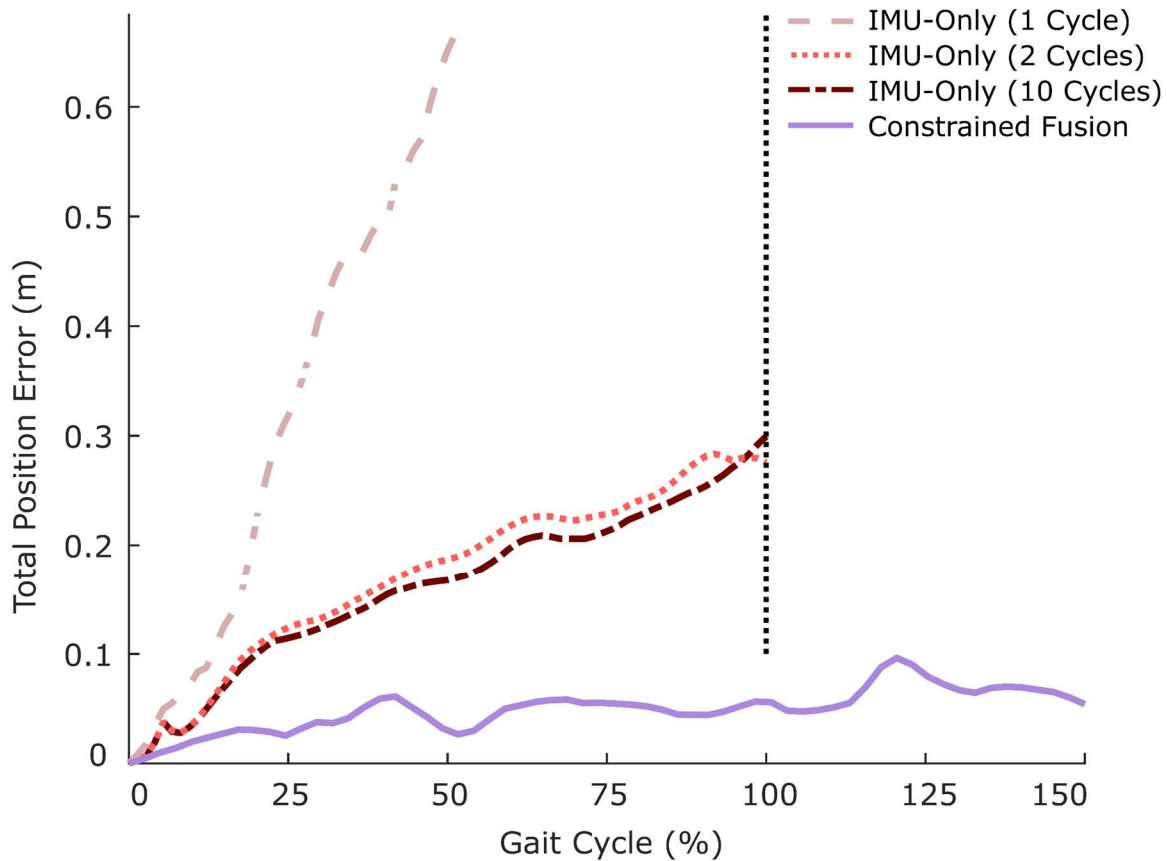
539

540 **Fig. 3. Comparison of Markerless Approaches.** Fusion approaches result in lower mean per joint (MPJ) angle root-
 541 mean-square errors (RMSEs) (top left) than the vision-only approach and lower MPJ position RMSEs (top right) than
 542 the IMU-only approach when tested on experimental data from the Total Capture dataset. Fusion methods resulted in
 543 better accuracy than single modality methods by maintaining consistent accuracy with respect to both joint angles and
 544 joint center positions across all individual joints. (*p < 0.05)



545

546 **Fig. 4. Sensitivity of Fusion Approaches to Noise.** Dynamically constrained fusion was advantageous at lower IMU
 547 accuracies and higher keypoint accuracies, whereas unconstrained fusion was advantageous at higher IMU
 548 accuracies and lower keypoints accuracies. This phenomenon occurs due to the sometimes complementary, but sometimes
 549 redundant nature of IMU data and modeling constraints since both provide information on the first and second order
 550 derivatives of the body segment motions. Mean \pm standard deviation is plotted here with * $p < 0.05$.



557

558 **Fig. 6. Error Accumulation with IMU Methods.** Observing the full body joint center position error over the gait cycle
559 reveals that dynamically constrained fusion and the other techniques eventually reach an equilibrium error, while the
560 IMU-only dynamic optimization continues to accumulate error throughout the simulation duration regardless of the
561 starting IMU data accuracy or the level of denoising. All other approaches can also be run for any arbitrary amount of
562 time, but IMU-only is restricted to complete gait cycles if the periodicity assumption is implemented to reduce drift.
563 However, the rate of error accumulation can be reduced by averaging over multiple periodic gait cycles.